Open Ceramics 17 (2024) 100566

Contents lists available at ScienceDirect

Open Ceramics

journal homepage: www.sciencedirect.com/journal/open-ceramics

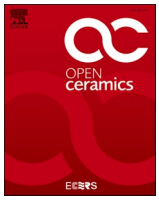

# Densification of hydroxyapatite through cold sintering process: Role of liquid phase chemistry and physical characteristic of HA powder

Muthusundar Kumar [a,b,*], Mohamed Aymen Ben Achour [b], Marie Lasgorceix [b], Paulo Quadros [c], Rosica Mincheva [a], Jean-Marie Raquez [a], Anne Leriche [b]

[a] Laboratory of Polymeric and Composite Materials, Centre of Innovation and Research in Materials and Polymers, University of Mons, Place Du Parc 23, 7000, Mons, Belgium
[b] Université Polytechnique Hauts-de-France, INSA Hauts-de-France, CERAMATHS-DMP, F-59313, Valenciennes, France
[c] FLUIDINOVA S.A., Rua de Rosa Jacome Felguerias, 57, 4475-188, Maia, Portugal

ARTICLE INFO

Handling Editor: P Colombo

*Keywords:*
Non-conventional sintering
Cold sintering process
Nano hydroxyapatite
Liquid chemistry
Densification

ABSTRACT

Hydroxyapatite is a well-known bioactive material widely employed in bone regeneration applications. Densifying hydroxyapatite at the nanoscale remains challenging with conventional sintering methods. This investigation focuses on the densification of commercially available nano-hydroxyapatite powders through the cold sintering process, utilizing water, acetic acid, and phosphoric acid solutions as transient liquids under 360 MPa pressure at 200 °C. The study systematically examines the influence of physical parameters of hydroxyapatite powder, liquid nature, and ionic concentrations of acid solutions on densification and microstructural characteristics. The relative density of consolidated samples varied with respect to the ionic concentration of the acid solution. Notably, a maximum relative density of 90% has been achieved for hydroxyapatite cold sintered using 2 M phosphoric acid solution without changing the original phase of hydroxyapatite. Overall, this study offers valuable insights into the impact of liquid chemistry on the densification of hydroxyapatite using the cold sintering technique.

## 1. Introduction

Hydroxyapatite (HA), due to its chemical and structural resemblance to natural bone minerals, has found widespread use in orthopaedics and dentistry [1,2]. HA chemically known as calcium phosphate with the formula of $Ca_{10}(PO_4)_6(OH)_2$, possesses key attributes such as bioactivity, biocompatibility, and osteoconductivity, making it an inevitable choice for biomedical applications, particularly in bone regeneration and drug delivery [3,4]. In general, HA bioactivity depends on different factors such as grain/crystal size, degree of crystallinity, Ca/P ratio, and microporosity [5]. In recent times, nano-sized HA, in both powder and consolidated form, has gained significant attention in orthopaedic implants owing to its enhanced mechanical and biological properties compared to micron-sized HA [6,7]. *In-vitro* and *in-vivo* experiments have demonstrated that under physiological conditions, nanostructured HA grains dissolve more rapidly and enhance bio-mineralization as well as cell differentiation compared to micro-grain HA [8,9]. Therefore, nano HA helps to expedite the formation of a bioactive layer and promotes osteointegration. These processes are vital for faster bone regeneration [10]. Considering these advantages, nano HA is an ideal candidate for developing bioceramic implants that are expected to offer superior biological and mechanical properties. However, densifying HA on the nanoscale is quite challenging through conventional sintering techniques [11].

It is well known that densifying HA ceramic compacts through conventional high-temperature sintering processes typically requires temperatures exceeding 1000 °C and a longer holding period, often several hours. Besides the high energy and time consumption associated with conventional sintering, it promotes uncontrolled grain growth, alters stoichiometry through element evaporation, and might eliminate the hydroxyl groups. This will directly impact the biological activity of densified HA ceramics [12–14]. To overcome the adverse effects of conventional sintering and to facilitate the densification of HA at the nanoscale, the recent advancements in sintering technologies have provided an innovative platform through the cold sintering process [15].

The cold sintering process (CSP) is a non-conventional, low-energy

* Corresponding author. Laboratory of Polymeric and Composite Materials, Centre of Innovation and Research in Materials and Polymers, University of Mons, Place du Parc 23, 7000 Mons, Belgium.
*E-mail addresses:* muthusundar.kumar@umons.ac.be, muthusundark@gmail.com (M. Kumar).

https://doi.org/10.1016/j.oceram.2024.100566
Received 7 December 2023; Received in revised form 1 March 2024; Accepted 1 March 2024
Available online 2 March 2024

sintering technique that promotes the densification of ceramics in the presence of transient liquids under low temperatures (<300 °C) and pressures up to ≤600 MPa [16]. Diverse categories of ceramics, including composites in bulk and multilayer forms, have been successfully densified through the cold sintering process using suitable transient liquids [17–19]. Additionally, it provides a flexible strategy for integrating materials of different thermal features such as polymers and metals into ceramics, which not being feasible through conventional methods [20,21]. In the context of cold sintering, the use of transient liquids plays a crucial role by providing a diffusion path for ions and molecules partially dissolving at the ceramic surface. Furthermore, the application of pressure and temperature drives the mass transport across grain boundaries through the pressure solution creep mechanism, facilitating particle rearrangement, precipitation, and recrystallization during cold sintering [22,23].

Several recent studies have demonstrated the advantages of the cold sintering process in densifying HA ceramics [24–28]. The literature provides evidence of successful densification, achieving relative densities of up to 97%, for iodine-substituted HA [24], freshly prepared HA, and commercial HA with three different particle sizes. This densification was indeed accomplished without the use of any liquids, under high pressures (≧500 MPa), which diverges from the classical dissolution-precipitation mechanism in CSP [25,26]. Later, Shen et al. revealed the underlying mechanism by comparing the cold sintering of freshly prepared HA, as well as commercial HA without using liquids. They proposed that the presence of adsorbed or lattice water in the HA contributes to the formation of hydrogen bonds between the particles, thereby facilitating the densification exclusively under high pressure [25]. To address the negligible solubility issue of HA in water, Shen et al. demonstrated the simultaneous synthesis and densification of HA with $CaHPO_4{\cdot}2H_2O$ and $Ca(OH)_2$ as an alternative [28]. However, the cold sintering of HA relies on the pressure solution creep mechanism, involving dissolution, diffusion, and precipitation. In this context, the dissolution/precipitation step is crucial and notably influenced by the liquid phase chemistry and the material's solubility. Abdullah et al. have emphasized this influence while investigating the effect of liquid phase chemistry on the densification of ZnO under CSP [29]. In line with the aspect mentioned above, Anna et al. also reported the cold sintering of mussel shell-derived HA with different liquid phases, including ethylenediaminotetraacetic acid, acetic acid, and phosphoric acid [27]. Despite these advancements, the densification behaviour of HA relative to the liquid phase chemistry and ionic concentration of liquid phases, regardless of pressure or temperature in cold sintering, remains poorly understood. Hence, there exists a necessity to uncover the role of liquid-phase chemistry during the cold sintering of HA.

From the dissolution-recrystallization viewpoint, it is essential to take into account the dissolution behaviour of HA, which is the first stage in cold sintering [22]. Many researchers have extensively investigated the dissolution kinetics of HA in water, acids, and buffer mediums [30–33]. Consequently, several mechanisms have been proposed to describe the dissolution kinetics. The HA dissolution is known to be faster in acidic pH through the incongruent dissolution mechanism (equation (1)) than in neutral or alkaline pH, which leads to the formation of thermodynamically metastable clusters, like Posner cluster or amorphous calcium phosphate (ACP) at the crystal surface [34,35].

$$Ca_6(PO_4)_6(OH)_2 \underset{\Leftrightarrow}{H^+} Ca_{2-x}(HPO_4)_x(PO_4)_{6-x}(OH)_{2-x} + Ca^{2+}\text{aq} + HPO_4^{2-}\text{aq} \quad (1)$$

Even though the dissolution experiments have been conducted in solutions with low solid content, it is important to note that dissolution kinetics and mechanism are influenced by critical factors including pKa, nature, and concentration of ions [34].

Based on those aforementioned considerations, the present study aimed to explore the role of liquid phase chemistry in cold sintering of HA ceramics under a moderate pressure of 360 MPa using acetic acid (weakly ionizable organic solvent), phosphoric acid (a strongly ionizable inorganic solvent) and water (auto ionizable amphoteric solvent) as transient liquids. Special attention has also been paid to studying various physical parameters of the HA powder and the ionic concentration of the chosen liquids on the densification and microstructure evolution during the cold sintering of commercial hydroxyapatite powders.

## 2. Materials and methods

### 2.1. Hydroxyapatite powders

Cold sintering experiments were carried out with commercially available nano HA powders (nanoXIM.HAp201 & HAp202, CAS 12167-74-7) supplied by FLUIDINOVA S.A. Both powders consist of aggregated nano HA particles with identical physical properties, but they have different aggregate sizes as given in Table 1. The rationale behind the selection of these commercial HA powders (HAp201 & HAp202) relies on their favourable physical properties such as surface area, tap density (Table 1), and particle morphology (Fig. 5). Some reports assert that these factors exert a considerable influence on the densification of HA through the cold sintering process [35,36]. Additionally, these powders are well-suited for making composites with polymers due to their good flowability and dispersibility in liquids and polymer systems [37]. Furthermore, the consistent production and cost-effectiveness make those commercial HA powders a choice for our present and future studies.

### 2.2. Cold sintering of hydroxyapatite

Fig. 1 shows the experimental procedure and cold sintering setup used to densify the HA powders. To initiate the process, approximately 1 g of the HA powder was individually wetted with different transient liquid phases through manual mixing. This was achieved by adding 10 wt% of the respective liquids, including distilled water, as well as three different concentrations (0.5, 1.0, & 2.0 M) of phosphoric ($H_3PO_4$ 85 wt % in $H_2O$, CAS 7664-38-2, AppliChem PanReac) and acetic acid ($CH_3COOH$, CAS 67-64-1, Carlo Erba Reagents) solutions using a pestle and mortar. Subsequently, the moistened HA powders were then transferred into a cylindrical steel die with a 13 mm inner diameter. The HA powders were insulated from direct contact with the piston surface using a 13 mm diameter kapton polyimide sheet to avoid contamination. A heating jacket was fitted around the die and a thermocouple was connected laterally to regulate the heating rate. The process began at room temperature, where the moistened HA powder was subjected to uniaxial compression using a mechanical testing machine in compression mode (Zwick Roell model Retroline 1185 with a 100 kN load cell) at 360 MPa (7 kN/min head speed) with 15 min holding time. Subsequently, the sample was heated up to 200 °C (5 °C/min) and held for 10 min. Displacement versus time was recorded during the compression, utilizing the machine's built-in displacement transducer sensor to monitor density evolution during the CSP. The recorded displacement data were used for comparison without the correction for thermal expansion of the die. After cooling to nearly 60 °C, the applied pressure

**Table 1**
Physical properties of commercial hydroxyapatite (HAp201 & HAp202) and calcined HAp202 powders.

| Parameters | | HAp201 | HAp202 | HAp202_600 | HAp202_900 |
|---|---|---|---|---|---|
| BET SSA ($m^2/g$) | | 98.02 | 97.75 | 39.08 | 8.20 |
| Tap density (g/ml) | | 0.57 | 0.80 | – | – |
| True density ($g/cm^3$) | | 2.93 | 2.96 | 3.09 | 3.14 |
| Particle aggregate size distribution (μm) | $D_{10}$ | 1.67 | 1.82 | 1.69 | 1.40 |
| | $D_{50}$ | 2.82 | 5.71 | 5.42 | 4.98 |
| | $D_{90}$ | 5.25 | 16.21 | 15.96 | 15.20 |
| Crystallite size (nm) | | 32 ± 2 | 32 ± 2 | 36 ± 2 | 63 ± 2 |

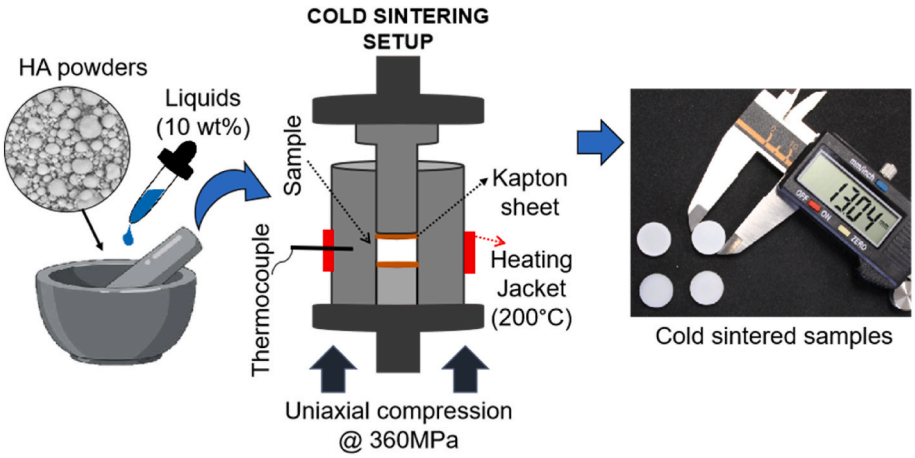


**Fig. 1.** Experimental procedure involved in the densification of HA through the cold sintering process.

was released, and then the densified samples were ejected from the die. In this way, the cold sintering experiment was done without the addition of any liquids for comparison purposes. For ease of convenience, the cold sintered samples were named upon the liquid tested as follows, CSP-W/L for the experiment without liquids, CSP-$H_2O$, CSP-AcOH and CSP-$H_3PO_4$ for the samples densified using water, acetic acid and phosphoric acid as transient liquids.

### 2.3. Characterizations

The apparent density of cold sintered samples, including the open porosity, was measured according to Archimedes' principle through hydrostatic weighing with water as the immersion liquid. Before the test, samples were kept in an oven at 110 °C overnight. For each experiment, a minimum of three samples were tested, and the average value was used in the calculation of relative density, as specified in Equation (2). To compute the relative density, the true density of HA powders measured using a Helium pycnometer Accypyc III (Micromeritics, USA), was taken into account.

$$\rho_r = \frac{m_{air} \times \rho_l}{m_{liq/air} - m_{liq/liq}} \times \frac{100}{\rho_T} \tag{2}$$

where, $m_{air}$ stands for the mass of the dry sample in air, $m_{liq/air}$ represents the mass of the water-immersed sample weighed in air, $m_{liq/liq}$ represents the mass of the water-immersed sample weighed in water, $\rho_l$ & $\rho_T$ is the density of immersion medium & true density of HA powder respectively.

The particle size distribution of the HA powders was quantified with the laser particle sizer method, using Malvern Mastersizer 3000 equipment. To determine the specific surface area (SSA) of both HA powders and cold sintered samples, the Brunauer-Emmett-Teller (BET) method was applied, employing the Micromeritics TriStar II equipment. Before the BET analysis, the powders underwent a 12 h degassing process at 200 °C. Similarly, for the cold-sintered HA samples, the pellets were fragmented into micron-sized chunks before analysis. The phase purity of HA powders, both cold sintered and conventionally sintered samples were characterized by powder X-ray diffraction analysis. The diffraction pattern was recorded in the 2θ angle range from 20 to 70°, with a scan step size of 0.013°, utilizing the Panalytical X'Pert pro diffractometer equipped with Cu Kα ($\lambda_{Cu} = 1.542$ Å) radiation at 40 Kv and 40 mA. The lattice parameters along the *a* and *c*-axis for the HA before and after cold sintering were determined according to Equation (3), considering the diffraction planes with Miller indices (002) and (300).

$$\frac{1}{d^2} = \frac{4}{3}\left(\frac{h^2 + hk + l^2}{a^2}\right) + \frac{l^2}{c^2} \tag{3}$$

Where d represents the distance between the crystal planes obtained from XRD results at the (002) and (300) Miller plane.

Morphological and microstructural assessments of HA powders and cold-sintered/conventionally sintered HA were conducted using a Hitachi SU5000 scanning electron microscope (SEM). For cold sintered samples, SEM observations were performed on the fractured surface coated with a platinum layer of a few nm thickness. For conventionally sintered samples, SEM observations were carried out after polishing and thermal annealing at 1100 °C, followed by metallization. The average grain size of conventionally sintered samples was calculated with ImageJ software by measuring at least 100 grains. The chemical structure of HA powder before and after cold sintering with different liquids was assessed from FTIR analysis. These analyses were carried out using Bruker IFS 66 V/S spectrometer (ATR-FTIR mode) from 4000 to 530 $cm^{-1}$ wavenumber range in transmittance mode with a resolution of 4 $cm^{-1}$. To assess the Ca/P ratio of HA before and after cold sintering, a micro XGT-9000 (Horiba scientific) X-ray fluorescence spectrometer was employed at an accelerated voltage of 50Kv with a spot size of 100 μm. Before XRF analysis, the HA powder was pelleted by pressing under 2 MPa pressure, and the cold sintered samples were used as such. For each sample, chemical composition was quantified from five different spots under vacuum and the average values were presented. The representative image of the spot made for XRF analysis was given in supplementary information (Fig. S1). Thermogravimetric analysis was carried out using a TGA Q500 (TA instruments) at a heating rate of 10 °C/min, ranging from room temperature to 800 °C under a nitrogen atmosphere.

## 3. Results and discussions

### 3.1. Conventional sintering and microstructure

As the HA particles are at the nanoscale in both the commercial HA powders, the impact of particle morphology and aggregate size on the conventional sintering density and microstructural features were examined. The sintering cycle was deduced from the linear shrinkage profile (Fig. 2(b)) obtained from the dilatometric measurements. The onset of linear shrinkage at 600 °C results from the elimination of nano-porosity within the aggregated particles and is completed between 890 and 900 °C. The elimination of open porosity within the green compact commences at 1000 °C and the complete densification is realized at 1200 °C. Under this understanding, the uniaxially compacted (2 ton) cylindrical HA green pellets (φ = 13 mm) were conventionally sintered in a programmable Nabertherm furnace at 1200 °C (5 °C/min) for 2 h. Driving through the conventional sintering mechanism both the samples HAp201 & HAp202 achieved a relative density of around 95%. The

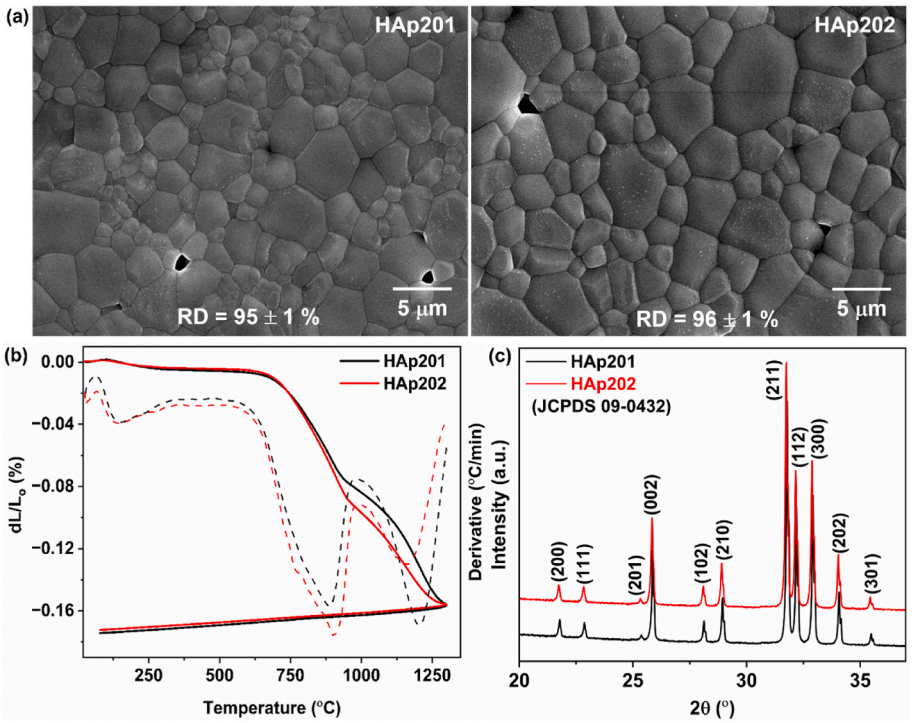


**Fig. 2.** (a) SEM images (b) dilatometry curve (dash lines represent the first derivative of the corresponding linear shrinkage curve), and (c) X-ray diffraction patterns of conventionally sintered commercial hydroxyapatite (HAp201 & HAp202).

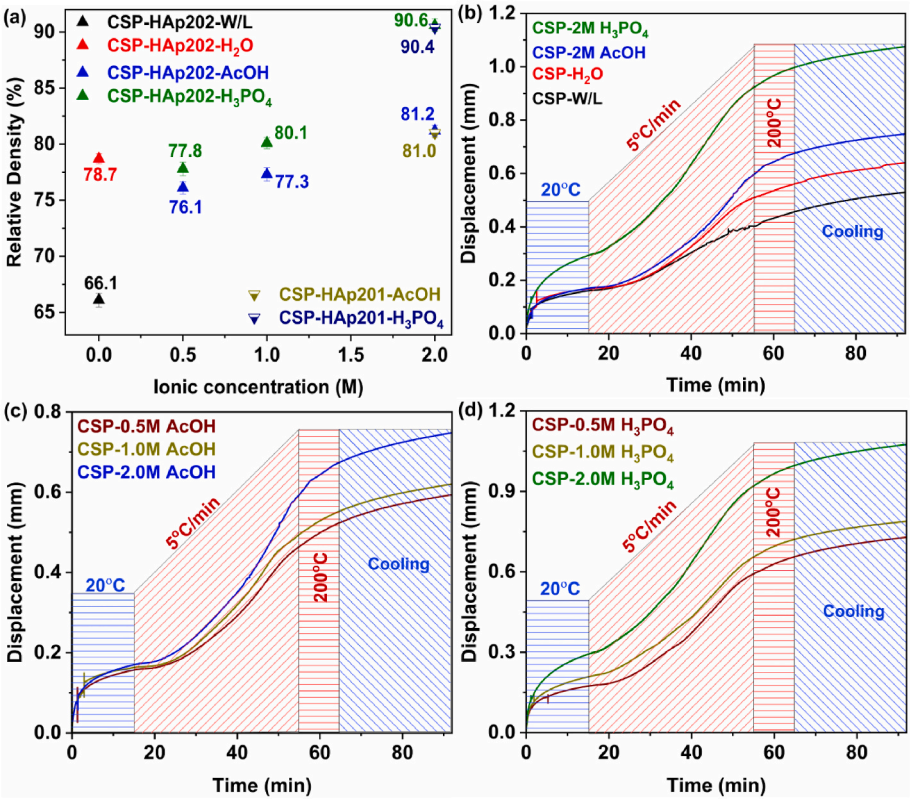


**Fig. 3.** (a) Relative density values obtained for densified HA corresponding to liquids solutions and their concentrations in CSP. Comparison of linear shrinkage profile obtained during the CSP under 360 MPa at 200 °C (b) without liquids, with water, 2 M AcOH and $H_3PO_4$ solution, (c) with different concentrations of AcOH solution, and (d) with $H_3PO_4$ solution. The measured volume shrinkage profile represents the total displacement not including a correction for the thermal expansion of the die.

calculated relative density values reveal that the particle aggregate size has a negligible influence on densification, although it could affect the grain growth dynamics [38,39]. The microstructure (Fig. 2(a)) of HAp202 consists of larger grains than HAp201. The average grain size was found to be 1.83 ± 0.52 and 2.10 ± 0.68 μm for HAp201 and HAp202, respectively. Interestingly XRD patterns in Fig. 2(c) evidenced that the conventional sintering process did not induce the decomposition of the HA phase or the formation of any secondary phases like tricalcium phosphate (α-TCP). On the other hand, conventional sintering promotes uncontrolled grain growth, to accomplish successful densification it requires several hours and consumes more energy [11].

### 3.2. Liquid phase chemistry in CSP of HA

The influence of liquid phase chemistry on achieving densification through a cold sintering process was experimented with HAp202 powder using water, aqueous solutions of $H_3PO_4$, and AcOH of three different ionic concentrations as well as without using any liquids. The calculated relative density values are given in Fig. 3(a). The cold sintered sample without the use of any liquids exhibited a relative density of approximately 66 %. Conversely the cold sintering of HA with transient liquids, a significant improvement in relative density was observed compared to the CSP without using any liquids. Like the HA samples cold sintered using aqueous acids, the relative density was varied with respect to the concentration of the respective acid solutions. Notably, the phosphoric acid solution promotes more effective densification than the acetic acid solution across the tested concentrations. Overall, the 2 M phosphoric acid solution promotes more densification than other liquids. However, at low acid solution concentrations (0.5 M), the relative densities show no significant improvement over the use of water as a transient liquid. Given the observed effectiveness of 2 M phosphoric acid solution in promoting densification, the cold sintering of HAp201 was assessed using 2 M acetic and phosphoric acid. The measured relative density values for HAp201 (Fig. 3(a)) were similar to the values obtained for HAp202. Thus it can be concluded that the particle aggregate size of HA has no significant role in the densification through the cold sintering process.

The role of liquids in the density evolution can be observed through the volumetric shrinkage profile, which is depicted in terms of displacement during the cold sintering process in Fig. 3(b, c & d). By comparing the cold sintering process without using liquids, water, 2 M AcOH, and $H_3PO_4$ solution (Fig. 3(b)), the initial volume shrinkage during the 15 min hold time under 360Mpa pressure is a result of particle rearrangement and contact flattening [40]. As the heating ramp starts, the dissolution process begins and continues until the saturation to promote mass transport across grain boundaries [29]. In the case of cold sintering without liquids, the mass transport is facilitated through chemical interactions between the adsorbed water molecules on the HA particles and this phenomenon contributes to the evolution of density [25]. On the contrary, the HAp201 powder contains around 5.6% adsorbed water molecules indicated by weight loss up to 200 °C (Fig. 7 (b)). Despite this, no significant densification was found at 200 °C under 360 MPa pressure when liquids are not employed.

In the cold sintering of HA using water as a transient liquid, the added water molecules (10 wt%) have contributed to the density evolution, as the water molecule has an auto-ionizable tendency which drives the dissolution and promotes the mass transport across the HA surfaces as mentioned in Equation (1) [25]. When considering acidic aqueous liquids, the evolution of density is found to be strongly dependent on both the strength and nature of the ions present. It is well known that phosphoric acid ($pK_{a1} = 2.14$, $pK_{a2} = 7.21$, $pK_{a3} = 12.35$) is inherently stronger than acetic acid ($pK_a = 4.76$). Conversely, the pH depends on the concentration of acidic ions in the respective acid solutions. Thus the dissolution of HA into the transient liquid is strongly controlled by the pH of acetic acid and phosphoric acid solutions which in turn influence the final densification. That is why the relative density varies upon the concentration of acid solutions. This fact is supported by the volume shrinkage profile presented in Fig. 3(c and d) recorded for the cold sintering process carried out using acetic and phosphoric acid of three different concentrations.

Based on the aforementioned correlations, a generalized schematic representation of the cold sintering mechanism of HA is illustrated in Fig. 4. As described by equation (1), hydrogen ions play a crucial role in driving the dissolution of $Ca^{2+}$/P $O_4^{2-}$ ions from the HA surface. Under the action of pressure and temperature, these dissolved ions/particles generate a chemical gradient across the contacting particle surfaces. This gradient, in turn, promotes mass transport across grain boundaries. The dissolution process will continue until the solution reaches its boiling point or saturation level. The resulting supersaturated solution, containing $Ca^{2+}/PO_4^{2-}$ ions, leaves amorphous calcium phosphate at the HA crystal surface, which subsequently undergoes recrystallization into HA across grain boundaries [33,34]. This process gives rise to the coalescence of grain boundary, which progresses to the densification of HA through a pressure-assisted solution creep mechanism in CSP [40]. Therefore, phosphoric acid is found to be more effective than acetic acid or water in densifying nano HA through a cold sintering process.

### 3.3. Microstructure/morphological aspects

Fig. 5 demonstrates the morphology of the commercial HA powders (HAp201 & HAp202). Both the powders consist of fine micron-sized loosely aggregated nano HA particles. Comparatively, HAp201 powder consists of finer micron-aggregate particles than the HAp202 powder (Table 1). Despite this discrepancy, both HA powders have identical physical properties like specific surface area, true density, and crystallite size (Table 1). The presence of nano-sized crystals was further confirmed by the broader diffraction peaks from the XRD patterns reported in Fig. 7 (a).

Fig. 6 illustrates the microstructural features of the densified HAp202 powder through cold sintering without liquids, using $H_2O$, AcOH (2 M), and $H_3PO_4$ (2 M). SEM images provide clear evidence that the microstructure of cold-sintered samples is primarily composed of densely packed nanograins. However, the level of dense packing varies depending on the relative density of the samples, and the presence of nanopores contributes to the open porosity of these samples. Furthermore, the decrease in the SSA values of cold-sintered samples can be attributed to the dense packing and diffusion of grain boundaries between the nanograins. This phenomenon renders the interparticle porosity inaccessible for the nitrogen used in SSA measurement [35]. Comparatively, the HA cold sintered with 2 M $H_3PO_4$ holds an SSA value $< 10$ $m^2/g$, emphasizing its capability to enable higher densification than other liquids tested.

Irrespective of the relative density, well-diffused grain boundaries are observed among the nanograins, thus there is densification not compaction. The grain morphology appears somewhat similar for samples cold sintered with 2 M AcOH, $H_2O$, and without any liquids. In contrast, the surface area and grain morphology for the sample cold sintered with 2 M $H_3PO_4$ differs significantly from the other samples, indicating an effective dissolution process. Overall, the changes in grain morphology of HAp202 powders (as seen in Fig. 5(b)) are ascribed to the interplay of chemical and physical forces during the cold sintering process. Under the action of pressure (360 MPa), aggregates are broken down and rearranged into stacked lamellar grains with irregular edges. The dissolution process, induced by the temperature, pressure, and liquid phase, exerts a capillary force on the grain surface, facilitating the intergranular diffusion of ions [40]. This, in turn, leads to grain boundary diffusion and dense packing resulting from the liquid-assisted plastic deformation within the grains. Since dissolution primarily occurs at the grain surface, an increased level of dissolution is expected to produce an etched crystal surface [41,42]. Consecutively, the sample cold sintered with 2 M $H_3PO_4$ exhibits grains with blunt edges.

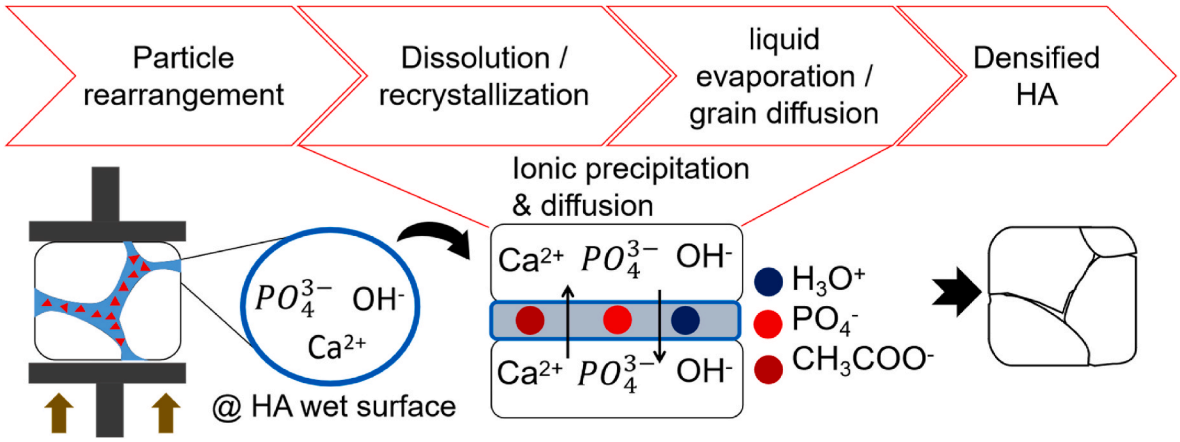


**Fig. 4.** Schematic illustration of the densification mechanism that occurs during the cold sintering of hydroxyapatite.

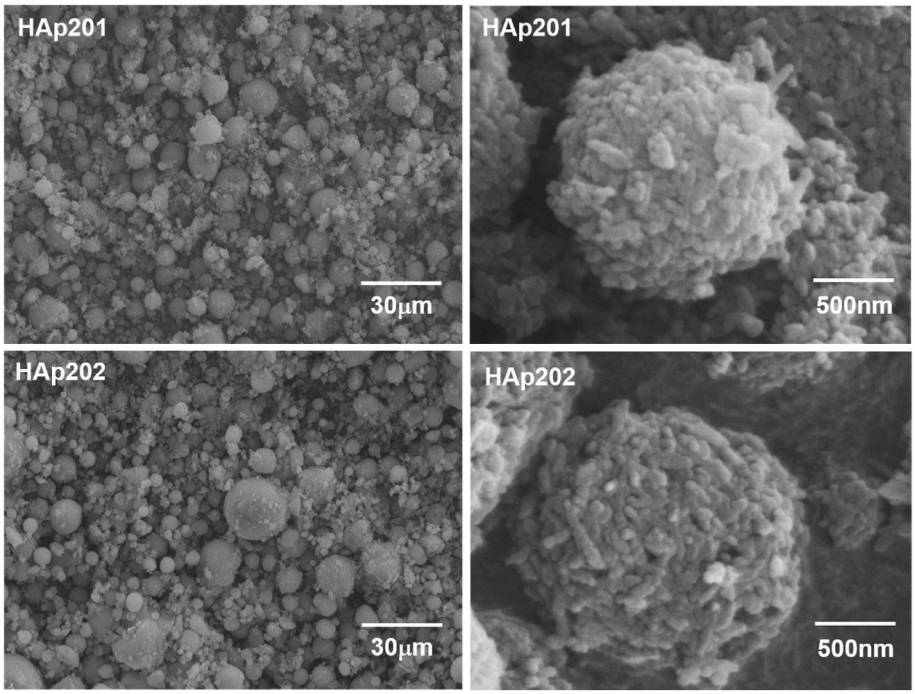


**Fig. 5.** SEM images of the commercial hydroxyapatite powders (HAp201 & HAp202).

Therefore, the choice of solvent is crucial in the cold sintering process to promote effective densification while preserving the particle grain size.

### 3.4. Phase and chemical structure

Although the acid solutions have effectively promoted the densification of HA compared to water, it is essential to assess the formation of any secondary phases. Powder XRD analysis was conducted on HAp202 powder as well as samples cold sintered using acetic and phosphoric acid (0.5 & 2.0 M) as well as water, and the obtained diffraction patterns are presented in Fig. 7(a). XRD pattern confirmed that the HAp202 powder is phase pure (JCPDS 00-024-0033) somewhat not fully crystalline. It is noteworthy that the agglomeration of HA particles during the spray drying process is achieved without the use of any polymer additives. Instead, the water present in the nano HA suspension acts as a binding agent to hold the particles together after the spray drying. The thermogram in Fig. 7(b) confirmed the aforementioned statement; the continuous weight loss of up to 650 °C was 6.9%, which stems from the removal of adsorbed and interstitial water molecules. Interestingly, the XRD patterns of all the analyzed cold sintered samples exhibit only diffraction peaks corresponding to the HA phase, similar to the HAp202 powder. Furthermore, the crystallite size of the samples remained consistent after cold sintering. Typically, crystal growth is associated with temperature, and it was expected that the use of a temperature of 200 °C in the cold sintering of HA would not encourage the crystal growth, primarily due to the dissolution and recrystallization process [30]. However, some slight changes in the lattice parameters along the a & c-axis were observed for the densified HA due to the ionic substitutions, and the results are provided in the supplementary information (Fig. S2) [43,44].

Based on the TGA results (Fig. 7(b)), it is evident that the HAp202 powder experiences a weight loss of approximately 4.3% up to 200 °C, attributed to the removal of adsorbed water molecules. In contrast, the mass loss up to 200 °C for the cold sintered samples, without liquid, with $H_2O$, 2 M AcOH, and 2 M $H_3PO_4$ was around 2.7, 2.5, 1.8, and 1.1% respectively. Despite the addition of 10 wt % of liquids, this mass loss is notably lower compared to the HAp202 powder. Comparing the mass loss between HAp202 and HA cold sintered without liquid and with

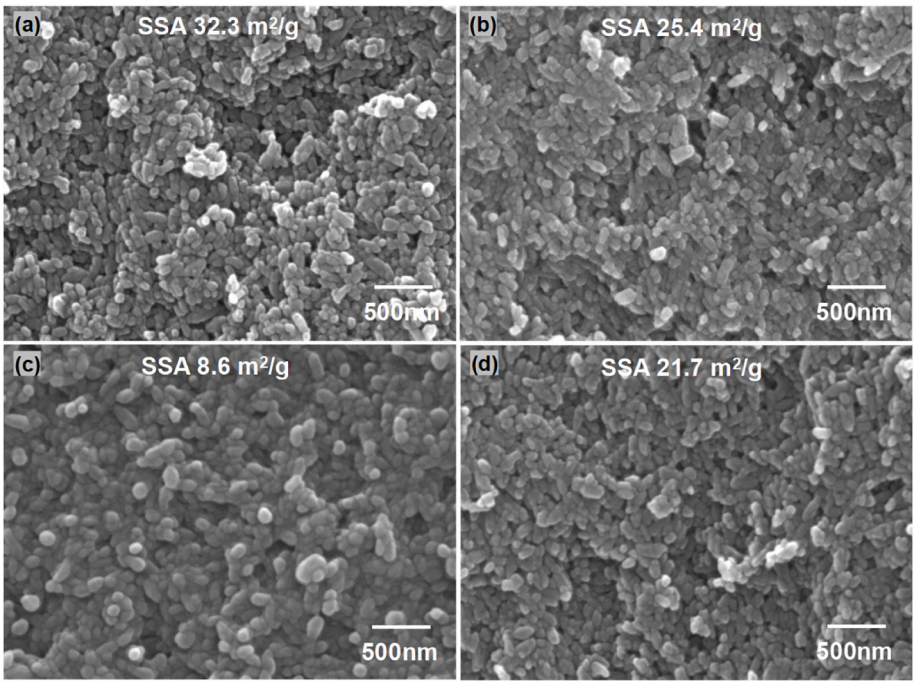


**Fig. 6.** SEM images of HAp202 powder cold sintered at 200 °C (a) without using liquids, (b) with $H_2O$, (c) with 2 M $H_3PO_4$ solution, and (d) with 2 M AcOH solution.

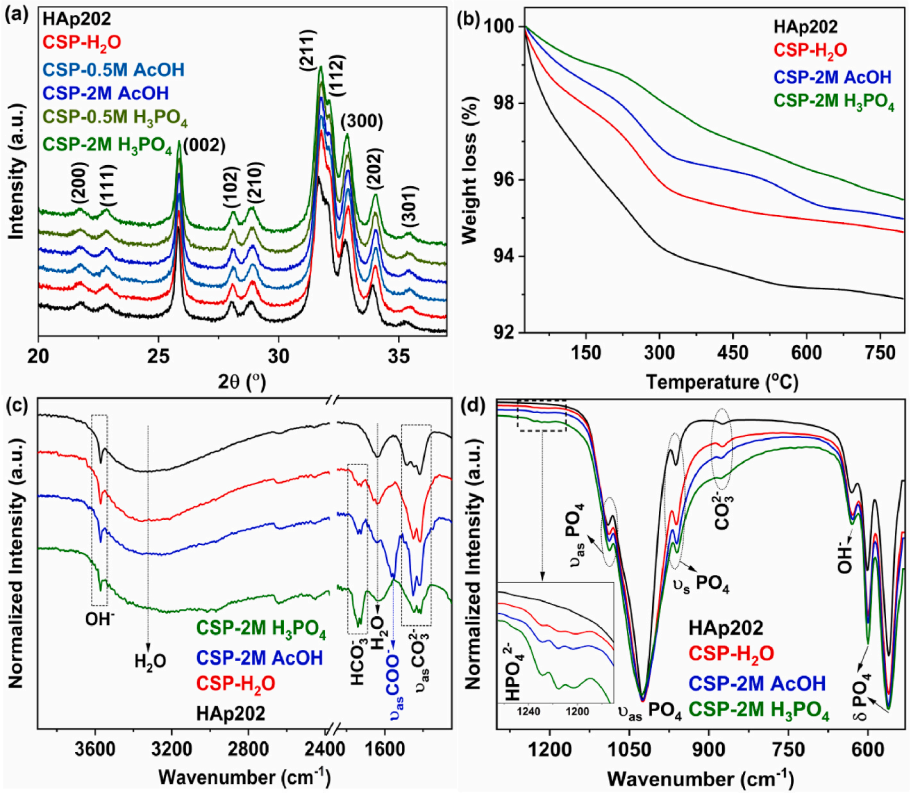


**Fig. 7.** (a) X-ray diffraction patterns of cold sintered HAp202 powder with $H_2O$, (0.5 & 2 M) AcOH and $H_3PO_4$ solution, (b) Thermogram of cold sintered HAp202 powder using $H_2O$, 2 M AcOH & $H_3PO_4$ solutions. FTIR patterns plotted (c) between wavenumber rage 4000 to 1250 $cm^{-1}$, and (d) between wavenumber rage 1250 to 530 $cm^{-1}$.

water, suggests that adsorbed water in HA likely participates in internal hydrolysis reactions such as the auto-ionization reaction of $H_2O$, facilitating densification before evaporating during the 10 min holding period at 200 °C [25,35]. In the case of acid solution, the introduction of acidic ($H^+$) ions enhances the extent of hydrolysis of adsorbed water. Consequently, this enhances dissolution-precipitation processes, ultimately leading to higher densification compared to HA cold sintered with water or without liquids. Hence the observed mass loss is

significantly lower for HA cold sintered with acid solutions.

The FTIR spectrum, recorded for HAp202 powder and samples cold sintered with $H_2O$, AcOH (2 M), and $H_3PO_4$ (2 M) are given in Fig. 7(c and d). The vibrational bands corresponding to $HCO_3^-$ (1700-1770 $cm^{-1}$), and $HPO_4^{2-}$ (1200-1250 $cm^{-1}$) in all the analyzed samples are ascribed to the ionic substitutions within the HA lattice [44,45]. The formation of $HCO_3^-$ results from the chemical reaction between $H^+$ ions from the liquid solutions and the type-B carbonates (1545-1400 $cm^{-1}$) adsorbed in the HA crystals [45,46]. In the case of HA densified with 2 M AcOH, the acetate ions are chemisorbed on the surface after cold sintering, indicating that the temperature of 200 °C is insufficient to decompose the organic residue. According to TGA measurements (Fig. 8 (b)), the chemisorbed acetate ions are found to be decomposed after 400 °C. In the cold sintered samples, relative to HA, the changes in the intensity and broadening of symmetric and asymmetric vibration peaks for $PO_4^{3-}$ groups suggest the substitution of non-apatite groups ($HPO_4^{2-}$) in the HA lattice [47,48]. These changes were more pronounced in the CSP-2M $H_3PO_4$ samples. The peak for lattice water (1640 $cm^{-1}$) in the $H_3PO_4$ sample appears broader, possibly due to the formation of H-bonding with the dissolved $PO_4^{3-}$ ions. Another possibility is that the $HPO_4^{2-}$ ions from the $H_3PO_4$ solution might occupy the site where $PO_4^{3-}$ ions dissolved from the HA lattice along the c-axis, forming hydrogen bonds with hydroxyl groups in HA. Moreover, TGA confirmed a consecutive weight loss after 350 °C for the $H_3PO_4$ sample, contributed by the loss of lattice water molecules and the thermal decomposition of non-apatitic groups [49]. Additionally, the deviation in the Ca/P ratio (supplementary information Fig. S3) for the CSP-2M $H_3PO_4$ sample in comparison to the stoichiometric ratio of 1.679 for HAp202 powders, suggests the inclusion of non-apatite groups from the phosphoric acid solution after cold sintering. Nonetheless, despite small changes in the crystal lattice parameters and stoichiometry, the use of 2 M $H_3PO_4$ promotes maximum densification of HA in CSP.

### 3.5. Influence of physical properties in CSP

In the context of cold sintering, dissolution-recrystallization is the chemical force exerted by liquids to facilitate densification under pressure and heat [22,23]. Therefore, surface area plays a crucial role by providing enough reaction sites for active ions in liquids to initiate the dissolution process. To verify this, the HAp202 powder underwent calcination aimed at removing the nano-porosity within the aggregated particles and water molecules. The onset and peak shrinkage points illustrated in the linear shrinkage curve (Fig. 2(b)) have guided the selection of the calcination temperature, 600 and 900 °C. The calcined HAp202 powder was then named HAp202_600 and HAp202_900. Following the calcination at these temperatures for 1 h with a ramp rate of 5 °C/min, a weight loss of around 3.96 and 6.27 % was observed at 600 and 900 °C respectively. Eventually, the changes in the particle aggregate size, specific surface area, and crystallite size relative to the calcination temperature (Table 1) serve as clear indicators of the loss of nano-porosity that leads to the shrinkage of particle diameter due to the pre-sintering effect [50]. Remarkably, the HAp202_900 powder is more completely crystalline than the HAp202_600 powder was confirmed by XRD patterns given in Fig. 8(a and b).

To assess the influence of the surface area and crystallinity of HA powders in CSP, experiments were conducted with HAp202 powder calcined at 600 and 900 °C using 2 M phosphoric acid solution as a transient liquid. The densified samples were then named as CSP-HAp202_600 and CSP-HAp202_900.

From the volume shrinkage profile (supplementary information Fig. S4), it is observed that the density evolution differs for both samples. The CSP-HAp202_600 sample achieved a relative density of around 82%, while the CSP-HAp202_900 sample reached around 68%. Importantly, the cold sintered pellet sample CSP-HAp202_900 remains structurally stable like other cold sintered samples during the density measurements conducted via hydrostatic weighing. This further implies the possibility of consolidation, not compaction. Furthermore, the XRD pattern (Fig. 8(a and b)) for the densified samples, revealed the presence

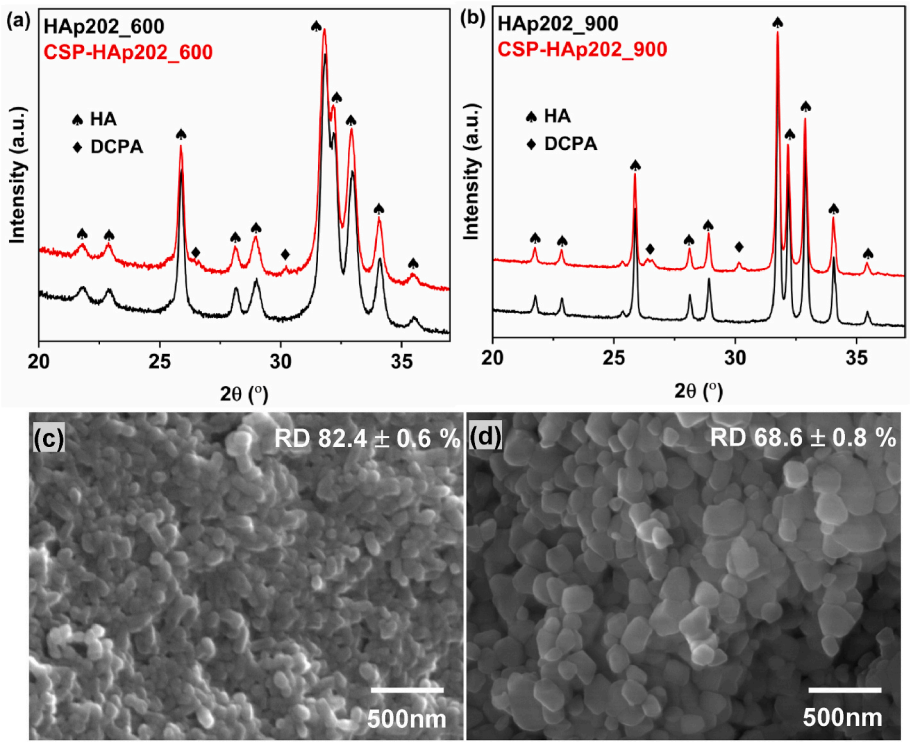


**Fig. 8.** (a & b) Comparative XRD patterns for the HAp202 calcined powders (600 & 900 °C) and cold sintered calcined HA powders at 200 °C using 2 M $H_3PO_4$ solution respectively. Microstructure of cold sintered (c) HAp202_600 powder, and (d) HAp202_900 powder.

of peaks corresponding to a secondary phase known as dicalcium phosphate ($CaHPO_4$, DCPA). This suggests that during CSP, the dissolved $Ca^{2+}$ ions might have reacted with $HPO_4^{2-}$ ions from the $H_3PO_4$ solution, subsequently recrystallizing as amorphous $CaHPO_4$. The XRD peak for DCPA in the CSP-HAp202_600 sample was relatively less intense than that in the CSP-HAp202_900 sample, suggesting that there was partial recrystallization of dissolved $Ca^{2+}/PO_4^{2-}$ ions into HA. While a few $Ca^{2+}$ ions precipitate/recrystallize into $CaHPO_4$ by reacting with $HPO_4^{2-}$ from phosphoric acid. This could be attributed to the surface area of the HAp202 powder calcined at 600 °C being quite higher than for HAp202 powder calcined at 900 °C (Table 1) [26]. Additionally, the former still contained an amorphous phase (adsorbed/lattice water), which facilitated effective dissolution and promoted more densification compared to the latter sample.

SEM images of the cold sintered samples HAp202_600 and HAp202_900 are given in Fig. 8(c and d), respectively. These images clearly illustrate that the densification is more pronounced in the case of the CSP-HAp202_600 sample. Although there is a visible difference in grain size and packing between both densified samples, the grains in both cases remain in the nano-range. The slightly larger grain size in CSP-HAp202-900 is a result of high-temperature calcination (900 °C). Furthermore, the HA grains in sample HAp202_900 sample are compacted and rearranged under the applied pressure. Additionally, the 2 M phosphoric acid dissolute $Ca^{2+}$ ions and re-precipitates them into amorphous $CaHPO_4$, which recrystallizes across the grain boundaries between the particles. Phase separation might also be associated with the crystallinity of the HAp202_900 powders [26]. Based on these findings, it can be concluded that the physical parameters such as surface area and crystallinity also influence the densification of HA through the cold sintering process. The fully crystalline HA with a low surface area was quite hard to densify through the cold sintering process.

## 4. Conclusions

Cold sintering of commercial hydroxyapatite powders was successfully demonstrated using water, and aqueous solutions of acetic and phosphoric acid as transient liquids by applying 360 MPa pressure at a temperature of 200 °C. The relative density was found to be increased with respect to the acidic strength of the corresponding liquids. This showed the significant influence of liquid phase chemistry on the densification of HA during the cold sintering process. Notably, the employment of 2 M phosphoric acid in the cold sintering of HA aided in achieving a maximum relative density of 90%. Furthermore, the XRD measurements and SEM observations confirmed the ability of the cold sintering process to preserve the original phase and grain size of hydroxyapatite even when acid liquids (2 M) were utilized. However, the use of 2 M $H_3PO_4$ slightly changes the lattice parameters and stoichiometry of HA, owing to the ionic substitution resulting from the dissolution-recrystallization process. Additionally, the cold sintering of calcined HA powder using 2 M phosphoric acid provided valuable insight into the impact of physical parameters such as surface area and crystallinity of HA on density evolution. Concurrently, the formation of the secondary phase $CaHPO_4$ served as evidence of the dissolution efficiency of phosphoric acid and illustrated the chemo-mechanical phenomenon driving densification in the cold sintering process. Overall this study offers valuable insights into the significance of liquid phase chemistry and physical properties of HA powders in the cold sintering process, particularly for achieving nano-level densification of bio-active ceramics.

## Declaration of competing interest

The authors declare that they have no known competing financial interests or personal relationships that could have appeared to influence the work reported in this paper.

## Acknowledgements

The authors wish to thank the Wallonia-Brussels Federation, Wallonia, and the EUNICE (European University for Customised Education) for general support in the framework of a joint PhD project between UMONS and UPHF. J.M. Raquez is a FRS-FNRS senior research associate. M. Kumar was so thankful to Mr. Gerard Moreau and Dr. Florian Jean for their assistance in SEM characterization. M. Kumar is also grateful to Dr. Stephane Hocquet and Dr. Charlotte Lang from the Belgian Ceramic Research Centre (CRIBC & INISMA) for providing facilities to do dilatometry and μ-XRF chemical analysis.

## Appendix A. Supplementary data

Supplementary data to this article can be found online at https://doi.org/10.1016/j.oceram.2024.100566.

## References

[1] S.M. George, C. Nayak, I. Singh, K. Balani, Multifunctional hydroxyapatite composites for orthopedic applications: a review, ACS Biomater. Sci. Eng. 8 (2022) 3162–3186, https://doi.org/10.1021/acsbiomaterials.2c00140.
[2] K. Pajor, L. Pajchel, J. Kolmas, Hydroxyapatite and fluorapatite in conservative dentistry and oral implantology—a review, Materials 12 (2019) 2683, https://doi.org/10.3390/ma12172683.
[3] E. Fiume, G. Magnaterra, A. Rahdar, E. Verné, F. Baino, Hydroxyapatite for biomedical applications: a short overview, Ceramics 4 (2021) 542–563, https://doi.org/10.3390/ceramics4040039.
[4] S. Mondal, U. Pal, 3D hydroxyapatite scaffold for bone regeneration and local drug delivery applications, J. Drug Deliv. Sci. Technol. 53 (2019) 101131, https://doi.org/10.1016/j.jddst.2019.101131.
[5] L. Wang, X. Luo, D. Barbieri, C. Bao, H. Yuan, Controlling surface microstructure of calcium phosphate ceramic from random to custom-design, Ceram. Int. 40 (2014) 7889–7897, https://doi.org/10.1016/j.ceramint.2013.12.136.
[6] H. Zhou, J. Lee, Nanoscale hydroxyapatite particles for bone tissue engineering, Acta Biomater. 7 (2011) 2769–2781, https://doi.org/10.1016/j.actbio.2011.03.019.
[7] M. Du, J. Chen, K. Liu, H. Xing, C. Song, Recent advances in biomedical engineering of nano-hydroxyapatite including dentistry, cancer treatment and bone repair, Compos. B Eng. 215 (2021) 108790, https://doi.org/10.1016/j.compositesb.2021.108790.
[8] C. Zhou, C. Deng, X. Chen, X. Zhao, Y. Chen, Y. Fan, X. Zhang, Mechanical and biological properties of the micro-/nano-grain functionally graded hydroxyapatite bioceramics for bone tissue engineering, J. Mech. Behav. Biomed. Mater. 48 (2015) 1–11, https://doi.org/10.1016/j.jmbbm.2015.04.002.
[9] C. Covarrubias, F. Arroyo, C. Balanda, M. Neira, A. Von Marttens, P. Caviedes, J. P. Rodríguez, C. Urra, The effect of the nanoscale structure of nanobioceramics on their in vitro bioactivity and cell differentiation properties, J. Nanomater. 16 (2015) 430, https://doi.org/10.1155/2015/526230. -430.
[10] X. Gui, W. Peng, X. Xu, Z. Su, G. Liu, Z. Zhou, M. Liu, Z. Li, G. Song, C. Zhou, Q. Kong, Synthesis and application of nanometer hydroxyapatite in biomedicine, Nanotechnol. Rev. 11 (2022) 2154–2168, https://doi.org/10.1515/ntrev-2022-0127.
[11] A. Indurkar, R. Choudhary, K. Rubenis, J. Locs, Advances in sintering techniques for calcium phosphates ceramics, Materials 14 (2021) 6133, https://doi.org/10.3390/ma14206133.
[12] G. Muralithran, S. Ramesh, The effects of sintering temperature on the properties of hydroxyapatite, Ceram. Int. 26 (2000) 221–230, https://doi.org/10.1016/S0272-8842(99)00046-2.
[13] R.A. Youness, M.A. Taha, M.A. Ibrahim, Effect of sintering temperatures on the in vitro bioactivity, molecular structure and mechanical properties of titanium/carbonated hydroxyapatite nanobiocomposites, J. Mol. Struct. 1150 (2017) 188–195, https://doi.org/10.1016/j.molstruc.2017.08.070.
[14] A. Karimzadeh, M.R. Ayatollahi, A.R. Bushroa, M.K. Herliansyah, Effect of sintering temperature on mechanical and tribological properties of hydroxyapatite measured by nanoindentation and nanoscratch experiments, Ceram. Int. 40 (2014) 9159–9164, https://doi.org/10.1016/j.ceramint.2014.01.131.
[15] H. Guo, A. Baker, J. Guo, C.A. Randall, Cold sintering process: a novel technique for low-temperature ceramic processing of ferroelectrics, J. Am. Ceram. Soc. 99 (2016) 3489–3507, https://doi.org/10.1111/jace.14554.
[16] H. Guo, J. Guo, A. Baker, C.A. Randall, Hydrothermal-assisted cold sintering process: a new guidance for low-temperature ceramic sintering, ACS Appl. Mater. Interfaces 8 (2016) 20909–20915, https://doi.org/10.1021/acsami.6b07481.
[17] A. Galotta, V.M. Sglavo, The cold sintering process: a review on processing features, densification mechanisms and perspectives, J. Eur. Ceram. Soc. 41 (2021) 1–17, https://doi.org/10.1016/j.jeurceramsoc.2021.09.024.
[18] H. Guo, A. Baker, J. Guo, C.A. Randall, Protocol for ultralow-temperature ceramic sintering: an integration of nanotechnology and the cold sintering process, ACS Nano 10 (2016) 10606–10614, https://doi.org/10.1021/acsnano.6b03800.

[19] J. Guo, R. Floyd, S. Lowum, J.P. Maria, T. Herisson de Beauvoir, J.H. Seo, C. A. Randall, Cold sintering: progress, challenges, and future opportunities, Annu. Rev. Mater. Res. 49 (2019) 275–295, https://doi.org/10.1146/annurev-matsci-070218-010041.
[20] J. Guo, X. Zhao, T. Herisson De Beauvoir, J.H. Seo, S.S. Berbano, A.L. Baker, C. Azina, C.A. Randall, Recent progress in applications of the cold sintering process for ceramic–polymer composites, Adv. Funct. Mater. 28 (2018) 1801724, https://doi.org/10.1002/adfm.201801724.
[21] J. Guo, S.S. Berbano, H. Guo, A.L. Baker, M.T. Lanagan, C.A. Randall, Cold sintering process of composites: bridging the processing temperature gap of ceramic and polymer materials, Adv. Funct. Mater. 26 (2016) 7115–7121, https://doi.org/10.1002/adfm.201602489.
[22] A. Ndayishimiye, M.Y. Sengul, T. Sada, S. Dursun, S.H. Bang, Z.A. Grady, K. Tsuji, S. Funahashi, A.C. Van Duin, C.A. Randall, Roadmap for densification in cold sintering: chemical pathways, Open Ceram 2 (2020) 100019, https://doi.org/10.1016/j.oceram.2020.100019.
[23] M. Biesuz, G. Taveri, A.I. Duff, E. Olevsky, D. Zhu, C. Hu, S. Grasso, A theoretical analysis of cold sintering, Adv. Appl. Ceram. 119 (2020) 75–89, https://doi.org/10.1080/17436753.2019.1692173.
[24] M. ul Hassan, H.J. Ryu, Cold sintering and durability of iodate-substituted calcium hydroxyapatite (IO-HAp) for the immobilization of radioiodine, J. Nucl. Mater. 514 (2019) 84–89, https://doi.org/10.1016/j.jnucmat.2018.11.024.
[25] H.Z. Shen, N. Guo, L. Zhao, P. Shen, Role of ion substitution and lattice water in the densification of cold-sintered hydroxyapatite, Scripta Mater. 177 (2020) 141–145, https://doi.org/10.1016/j.scriptamat.2019.10.024.
[26] M. ul Hassan, M. Akmal, H.J. Ryu, Cold sintering of as-dried nanostructured calcium hydroxyapatite without using additives, J. Mater. Res. Technol. 11 (2021) 811–822, https://doi.org/10.1016/j.jmrt.2021.01.060.
[27] A. Galotta, F. Agostinacchio, A. Motta, S. Dirè, V.M. Sglavo, Mechanochemical synthesis and cold sintering of mussel shell-derived hydroxyapatite nano-powders for bone tissue regeneration, J. Eur. Ceram. Soc. 43 (2023) 639–647, https://doi.org/10.1016/j.jeurceramsoc.2022.09.024.
[28] H.Z. Shen, N. Guo, Y.H. Liang, P. Shen, Synthesis and densification of hydroxyapatite by mechanochemically-activated reactive cold sintering, Scripta Mater. 194 (2021) 113717, https://doi.org/10.1016/j.scriptamat.2020.113717.
[29] A. Jabr, J. Fanghanel, Z. Fan, R. Bermejo, C. Randall, The effect of liquid phase chemistry on the densification and strength of cold sintered ZnO, J. Eur. Ceram. Soc. 43 (2023) 1531–1541, https://doi.org/10.1016/j.jeurceramsoc.2022.11.071.
[30] S.V. Dorozhkin, Inorganic chemistry of the dissolution phenomenon: the dissolution mechanism of calcium apatites at the atomic (ionic) level, Comments Mod. Chem. 20 (1999) 285–299, https://doi.org/10.1080/02603599908021447.
[31] S.V. Dorozhkin, Dissolution mechanism of calcium apatites in acids: a review of literature, World J. Methodol. 2 (2012) 1, 10.5662%2Fwjm.v2.i1.1.
[32] D. Wang, Y. Xie, D.P. Jaisi, Y. Jin, Effects of low-molecular-weight organic acids on the dissolution of hydroxyapatite nanoparticles, Environ. Sci.: Nano 3 (2016) 768–779, https://doi.org/10.1039/C6EN00085A.
[33] S.V. Dorozhkin, Surface reactions of apatite dissolution, J. Colloid Interface Sci. 191 (1997) 489–497, https://doi.org/10.1006/jcis.1997.4942.
[34] A.N. Smith, A.M. Posner, J.P. Quirk, Incongruent dissolution and surface complexes of hydroxyapatite, J. Colloid Interface Sci. 48 (1974) 442–449, https://doi.org/10.1016/0021-9797(74)90188-X.
[35] K. Rubenis, S. Zemjane, J. Vecstaudza, J. Bitenieks, J. Locs, Densification of amorphous calcium phosphate using principles of the cold sintering process, J. Eur. Ceram. Soc. 41 (2021) 912–919, https://doi.org/10.1016/j.jeurceramsoc.2020.08.074.
[36] S.K. Swain, S.V. Dorozhkin, D. Sarkar, Synthesis and dispersion of hydroxyapatite nanopowders, Mater. Sci. Eng. C 32 (2012) 1237–1240, https://doi.org/10.1016/j.msec.2012.03.014.
[37] B. Santhosh, A. Galotta, G.D. Sorarù, V.M. Sglavo, M. Biesuz, Cold sintering of colloidal silica particles using different alkali solutions, Ceram. Int. 48 (2022) 35627–35632, https://doi.org/10.1016/j.ceramint.2022.08.334.
[38] S. Ramesh, C.Y. Tan, S.B. Bhaduri, W.D. Teng, I. Sopyan, Densification behaviour of nanocrystalline hydroxyapatite bioceramics, J. Mater. Process. Technol. 206 (2008) 221–230, https://doi.org/10.1016/S0272-8842(99)00046-2.
[39] A. Bianco, I. Cacciotti, M. Lombardi, L. Montanaro, G. Gusmano, Thermal stability and sintering behaviour of hydroxyapatite nanopowders, J. Therm. Anal. Calorim. 88 (2007) 237–243, https://doi.org/10.1007/s10973-006-8011-6.
[40] W.D. Kingery, Densification during sintering in the presence of a liquid phase. I. Theory, J. Appl. Phys. 30 (1959) 301–306, https://doi.org/10.1063/1.1735155.
[41] W.L. Jongebloed, I. Molenaar, J. Arends, Orientation-dependent etchpit penetration and dissolution of fluoroapatite, Caries Res. 7 (1973) 154–165, https://doi.org/10.1016/0003-9969(66)90032-X.
[42] N.W. Johnson, Differences in the shape of human enamel crystallites after partial destruction by caries, EDTA and various acids, Arch. Oral Biol. 11 (1966), https://doi.org/10.1159/000259839, 1421-IN49.
[43] J.E. Hills, H.R. Sullivan, Studies on the acid decalcification of human dental enamel. I, Aust. Dent. J. 3 (1958) 6–18, https://doi.org/10.1111/j.1834-7819.1958.tb01812.x.
[44] E.I.F. Pearce, On the dissolution of hydroxyapatite in acid solutions, J. Dent. Res. 67 (1988) 1056–1058, https://doi.org/10.1177/00220345880670070801.
[45] M.S. Hossain, S. Ahmed, FTIR spectrum analysis to predict the crystalline and amorphous phases of hydroxyapatite: a comparison of vibrational motion to reflection, RSC Adv. 13 (2023) 14625–14630, https://doi.org/10.1039/D3RA02580B.
[46] S. Diallo-Garcia, M.B. Osman, J.M. Krafft, S. Casale, C. Thomas, J. Kubo, G. Costentin, Identification of surface basic sites and acid–base pairs of hydroxyapatite, J. Phys. Chem. C 118 (2014) 12744–12757, https://doi.org/10.1021/jp500469x.
[47] S.J. Joris, C.H. Amberg, Nature of deficiency in nonstoichiometric hydroxyapatites. II. Spectroscopic studies of calcium and strontium hydroxyapatites, J. Phys. Chem. 75 (1971) 3172–3178, https://doi.org/10.1021/j100689a025.
[48] E.E. Berry, The structure and composition of some calcium-deficient apatites, J. Inorg. Nucl. Chem. 29 (1967) 317–327, https://doi.org/10.1016/0022-1902(67)80033-2.
[49] S. Lazić, S. Zec, N. Miljević, S. Milonjić, The effect of temperature on the properties of hydroxyapatite precipitated from calcium hydroxide and phosphoric acid, Thermochim. Acta 374 (2001) 13–22, https://doi.org/10.1016/S0040-6031(01)00453-1.
[50] O.G. Agbabiaka, I.O. Oladele, A.D. Akinwekomi, A.A. Adediran, A.O. Balogun, O. G. Olasunkanm, T.M.A. Olayanju, Effect of calcination temperature on hydroxyapatite developed from waste poultry eggshell, Scientific African 8 (2020) e00452, https://doi.org/10.1016/j.sciaf.2020.e00452.